On the Appearance of Wrinkled Morphology for $Cs_xFA_{1-x}Pb(I_{1-y}Br_y)_3$ Perovskite Compositions and the Impact on Solar Cell Performance

Steffen Braunger,[1a] Laura E. Mundt,[2] Christian M. Wolff,[3] Mathias Mews,[1b] Carolin Reherman,[1c] Marko Jost,[1a] Alvaro Tejada,[1b,4] David Eisenhauer,[1d] Christiane Becker,[1d] Jorge Andrés Guerra,[4] Eva Unger,[1c] Lars Korte,[1b] Dieter Neher,[3] Martin C. Schubert,[2] Bernd Rech,[1b] Steve Albrecht*[1a]

[1] Helmholtz-Zentrum Berlin für Materialien und Energie GmbH; [a] Young Investigator Group Perovskite Tandem Solar Cells, [b] Institute of Silicon Photovoltaics, [c] Young Investigator Group Hybrid Materials Formation and Scaling, [d] Young Investigator Group Nano-SIPPE, Kekuléstraße 5, 12489 Berlin, Germany.

[2] Fraunhofer Institute for Solar Energy Systems ISE, Heidenhofstr. 2, 79110 Freiburg, Germany.

[3] University of Potsdam, Institute of Physics and Astronomy, Karl-Liebknecht-Str. 24-25, 14476 Potsdam-Golm, Germany.

[4] Departamento de Ciencias, Sección Física, Pontificia Universidad Católica del Perú, Av. Universitaria 1801, Lima 32, Peru.

Corresponding Author

*E-mail: steve.albrecht@helmholtz-berlin.de

ABSTRACT

We report on the formation of wrinkle-patterned surface morphologies in cesium formamidinium based $Cs_xFA_{1-x}Pb(I_{1-y}Br_y)_3$ perovskite compositions with x = 0–0.3 and y = 0–0.3 under various spin-coating conditions. By varying the Cs and Br content, perovskite precursor solution concentration, and spin-coating procedure, the occurrence and characteristics of the wrinkle-shaped morphology can be tailored systematically. $Cs_{0.17}FA_{0.83}Pb(I_{0.83}Br_{0.17})_3$ perovskite layers were analyzed regarding their surface roughness, microscopic structure, local and overall composition, and optoelectronic properties. Application of these films in p-i-n perovskite solar cells (PSCs) with $ITO/NiO_x/perovskite/C_{60}/BCP/Cu$ architecture resulted in up to 15.3% and 17.0% power conversion efficiency for the flat and wrinkled morphology, respectively. Interestingly, we find slightly red-shifted photoluminescence (PL) peaks for wrinkled areas and we are able to directly correlate surface topography with PL peak mapping. This is attributed to differences in local grain size, while there is no indication for compositional de-mixing in the films. We show that perovskite composition, crystallization kinetics, and layer thickness strongly influence the formation of wrinkles which is proposed to be related to the release of compressive strain during perovskite crystallization. Our work helps to better understand film formation and to further improve efficiency of PSCs with widely used mixed perovskite compositions.

INTRODUCTION

Hybrid metal halide perovskite photovoltaics have developed rapidly as is demonstrated by the rise in power conversion efficiency (PCE) records of small area solar cells from 3.9% to 22.7% within just eight years.[1–4] Exceptional optoelectronic properties,[5] band gap tunability,[6] solution processability[7] and natural abundance of raw materials promise perovskite solar cells (PSCs) at low cost,[8] which is particularly attractive for application in photovoltaics. The complementary absorption to crystalline silicon make perovskites a suitable candidate for tandem solar cells in combination with the established silicon photovoltaic technology.[9,10] $CH_3NH_3PbI_3$ (MAPbI$_3$)-based perovskite has enabled highly promising PSCs efficiencies,[2,11–13] but due to the volatile nature of methylammonium (MA) these materials are limited in thermal stability[14] and stability under illumination,[15] and thus long-term stability. Hence, most recent high-performance PSCs employ thermally more stable perovskite blends based on formamidinium lead iodide (FAPbI$_3$). However, pure FAPbI$_3$ exhibits a yellow photo-inactive δ-phase at ambient temperature,[16] and therefore MA, cesium, rubidium and bromide have been incorporated to stabilize the photoactive α-phase of FAPbI$_3$.[12,16–18] Moreover, perovskites containing cesium have shown improved crystallinity, photo stability, moisture tolerance and reduced current-voltage (*J–V*) hysteresis.[12,16,17,19] Cesium incorporation also allows band gap (E_g) tuning[20–22] with a summary of the optical data of a variety of compositions published by some of us recently.[6] Frequently employed mixed cation/anion perovskites for highly efficient PSCs are the so-called triple cation compositions $Cs_x(MA_yFA_{1-y})_{1-x}Pb(I_{1-z}Br_z)_3$,[12,16,23,24] or compositions without the volatile MA cation such as $CsPb(I_{1-y}Br_y)_3$[25] and $Cs_xFA_{1-x}Pb(I_{1-y}Br_y)_3$.[17,26–28] For the latter type of perovskite, high solar cell stability and excellent band gap fine tuning has been demonstrated.[17,27] Among these compositions, $Cs_{0.17}FA_{0.83}Pb(I_{0.83}Br_{0.17})_3$ perovskites with 1.63 eV band gap have been employed in the most efficient monolithic perovskite/silicon tandem solar cells to date.[26] However, little is yet known about the material and thin film related properties. To further

understand the structure-function relationship, more analyses of the respective films and solar cells fabricated with this composition are needed. In the aforementioned publication by Bush *et al.* AFM images with microscopically textured $Cs_{0.17}FA_{0.83}Pb(I_{0.83}Br_{0.17})_3$ perovskite layers were shown.[26] Very similar patterns have also been observed by Jacobsson *et al.*,[29] Kim et al.[28] and Sveinbjörnsson *et al.*[30] for a wide range of $MA_xFA_{(1-x)}Pb(I_{1-y}Br_y)_3$ perovskites. The latter authors described the pattern as highly ordered wrinkles, a term that will be adapted here. While the origin of this microstructure is subject of current discussion,[30,31] textured thin films have received great interest for enhancing photovoltaic performance: Micro- and nanostructured substrates or photoactive layers increase light scattering and enhance light in-coupling which can improve the short-circuit current (J_{sc}) as demonstrated in thin film silicon[32] and perovskite solar cells.[33,34] However, solution-processed deposition of thin charge selective contact layers on textured perovskite often results in performance loss from shunts and poor charge extraction.[26] Also, the film morphology itself plays a significant role in the corresponding performance metrics of perovskite solar cells.[33,35–38] Thus, we herein investigate key parameters that influence the formation of wrinkled perovskite films and compare their optoelectronic properties to perovskite layers of the same composition exhibiting a flat morphology. By carefully tuning the film processing parameters we can generate deliberately flat and wrinkled films (Figure 1b-g). Most recently we reported on the investigation of optical constants and band gaps of flat and wrinkled $Cs_{0.17}FA_{0.83}Pb(I_{1-x}Br_x)_3$ perovskite layers with x = 0–0.4 by variable angle spectroscopic ellipsometry and spectral transmittance.[39] That work and the present study were conducted simultaneously to a study on the appearance of wrinkles in $Cs_{0.17}FA_{0.83}Pb(I_{0.83}Br_{0.17})_3$ perovskite layers by McGehee and coworkers, also published very recently.[31] Besides analyzing the origin of wrinkle formation we here focus on the impact on perovskite layer morphology on the solar cell performance. For this we utilize p–i–n (so called inverted) perovskite solar cells with the perovskite absorber sandwiched between nickel oxide as the hole transporting contact and

fullerene-C_{60} as the electron selective contact with the architecture ITO/NiO$_x$/Cs$_{0.17}$FA$_{0.83}$Pb(I$_{0.83}$Br$_{0.17}$)$_3$/C$_{60}$/BCP/Cu, as shown in Figure 1a. We find that the wrinkled perovskite morphology enables higher open-circuit voltage (V_{oc}) and short-circuit current (J_{sc}) than its flat counterpart. To understand the impact of perovskite morphology on solar cell performance, we use information from photoluminescence (PL), energy-dispersive X-ray diffraction (EDX), X-ray photoelectron spectroscopy (XPS), and X-ray diffraction (XRD).
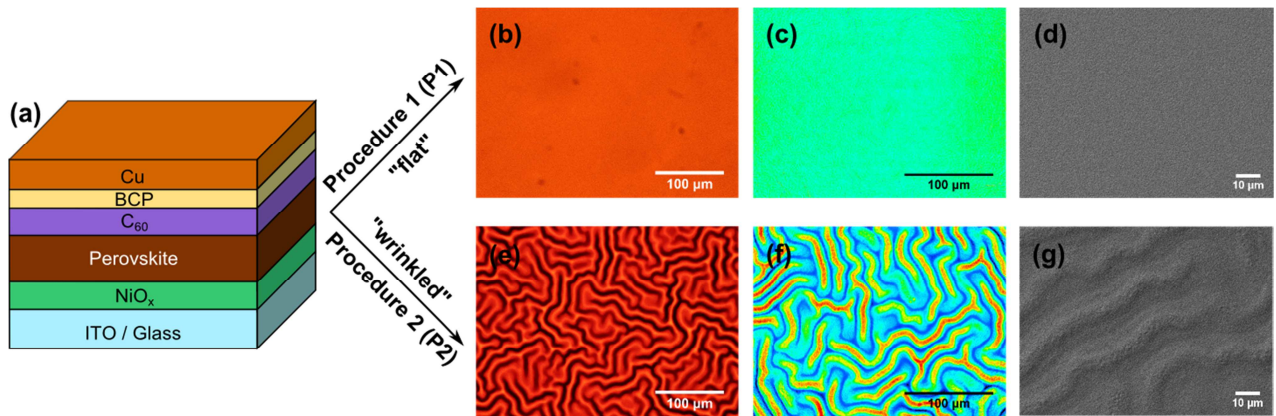

Figure 1: (a) Schematic illustration of the device architecture of perovskite solar cells fabricated in this work and (b-g) images of Cs$_{0.17}$FA$_{0.83}$Pb(I$_{0.83}$Br$_{0.17}$)$_3$ perovskite layers deposited under two different conditions (*P1* and *P2*; for details see Experimental Section). (b, e) Optical microscope images in transmission mode, (c, f) confocal microscope images, and (d, g) scanning electron microscopy images of perovskite layers.

METHODS

Materials. Chemicals were purchased from TCI (lead(II) iodide 99.99% Pb, lead(II) bromide 99.99% Pb), Sigma-Aldrich (bathocuproine 99.99%, fullerene-C_{60} 99.9%, ethylenediamine 99%, poly(methyl methacrylate) 120,000 M$_w$, anhydrous chlorobenzene, anhydrous dimethyl sulfoxide, anhydrous dimethylformamide), Alfa Aesar (nickel(II) nitrate hexahydrate 99.9985%, copper shot 99.999%, ethylene glycol 99%), ABCR (cesium bromide 99.999% Cs, cesium iodide 99.999% Cs) and Dyenamo (formamidinium iodide 98%), and were used as received. Indium-doped tin oxide (ITO)-coated glass substrates were purchased from Automatic Research GmbH

(25 × 25 × 11 mm, 15 Ω/□, patterned ITO) and Luminescence Technology Corporation (25 × 25 × 11 mm, 15 Ω/□, full area ITO).

Perovskite Solar Cell Fabrication. Planar p–i–n perovskite solar cells were fabricated as a layered stack of glass/ITO/NiO$_x$/Cs$_{0.17}$FA$_{0.83}$Pb(I$_{0.83}$Br$_{0.17}$)$_3$/C$_{60}$/BCP/Cu. Patterned ITO-coated glass substrates were cleaned in acetone, detergent (Mucasol 2 vol% in water), water and isopropanol in an ultrasonic bath for 15 min, respectively. Before layer deposition the substrates were dried in a N$_2$ stream and treated in an UV ozone cleaner (FHR Anlagenbau GmbH, UVOH 150 LAB) for 15 min. The NiO$_x$ layer was deposited by a sol-gel method, closely following the procedure from You et al.[40] A 1 M solution of nickel(II) nitrate hexahydrate in ethylene glycol with an equimolar amount of ethylene diamine was prepared and stirred for 10 min. After filtration through a 0.45 µm PVDF filter, the solution was spin coated onto ITO-coated glass at 8000 rpm for 60 s with an acceleration time of 3 s in air. The wet film was dried at 100 °C for 10 min followed by oxidation at 300 °C for 1 h in ambient conditions. The substrates were left to cool down and quickly transferred into a glovebox for deposition of all following layers under dinitrogen atmosphere. Cs$_{0.17}$FA$_{0.83}$Pb(I$_{0.83}$Br$_{0.17}$)$_3$ layers were deposited in close analogy to previously reported procedure for this perovskite composition.[17,26] A 0.9 M Cs$_{0.17}$FA$_{0.83}$Pb(I$_{0.83}$Br$_{0.17}$)$_3$ precursor solution was prepared by dissolving cesium bromide (57.9 mg, 0.153 mmol, 0.17 equiv.), formamidinium iodide (128.5 mg, 0.747 mmol, 0.83 equiv.), lead(II) bromide (56.2 mg, 0.17 equiv.) and lead(II) iodide (344.4 mg, 0.747 mmol, 0.83 equiv.) in a mixture of dimethylformamide and dimethyl sulfoxide (4:1 volume ratio, 880 µL). The precursor solution was shaken at 60 °C for 30 min and left to cool down to ambient temperature before use. Higher or lower concentrated perovskite precursor solutions were prepared in the same way by adjusting the volume of solvent mixture added. Two deposition procedures were used to obtain a perovskite layer with flat surface morphology (*Procedure 1, P1*) and wrinkled surface morphology (*Procedure 2, P2*). *P1*: Perovskite precursor solution (100 µL) was spread on

6

the substrate and spun at a single-step process with open spin coater lid, 4000 rpm for 30 s with an acceleration time of 1 s; during this process chlorobenzene (150 µL) was dripped from 1 cm distance on the center of the spinning substrate after 25 s. The perovskite layer was directly transferred on a hot plate for annealing at 100 °C for 20 min. *P2*: Perovskite precursor solution (100 µL) was spread on the substrate and spun at a two-step process with closed spin coater lid, 1000 rpm for 10 s with an acceleration time of 1 s followed by 6000 rpm for 30 s with an acceleration time of 3 s; during this process chlorobenzene (150 µL) was dripped from 1 cm distance on the center of the spinning substrate after 42 s. The spin coating time is 40 seconds plus 4 seconds acceleration; in total 44 s. Antisolvent quenching was done 2 s before the end of spin-coating, hence after 42 s. The perovskite layer was directly transferred on a hot plate for annealing at 50 °C for 1 min, then on a second hot plate at 100 °C for 20 min. After cooling to ambient temperature, the electron selective layer (fullerene-C_{60}), hole blocking layer (bathocuproine) and back electrode (Cu) were deposited in a thermal evaporator (M. BRAUN GmbH, MB-EcoVap) at a base pressure of $< 10^{-6}$ mbar. First, 25 nm fullerene-C_{60} was vacuum deposited at a source temperature of 370 °C and rate of 0.3 Å/s, then 6 nm BCP was deposited at a source temperature of 125 °C and rate of 0.5 Å/s, finally, 100 nm copper was deposited through a shadow mask, to define six active areas of 16 mm^2 on each substrate, at a rate of 0.1 to 1.0 Å/s.

Thin Film Characterization. *UV/vis/NIR Spectroscopy:* Reflectance and transmission spectra were recorded between 300 and 850 nm in 4 nm steps using a PerkinElmer Lambda 1050 UV/vis/NIR spectrometer, calibrated with a white Spectralon. The illumination beam size of this setup was 3.5×3.5 mm^2. *Microscopy:* Optical microscope images were recorded on a Leitz DMRX in transmission mode equipped with Canon EOS 700D camera. SEM images were recorded using a Hitachi S4100 or ZEISS Auriga 60 at 5 kV acceleration voltage and 10k×, 30k× and 50k× magnification. Grains sizes and layer thicknesses were determined using the software "ImageJ". Surface analysis was performed using a Park Systems XE-70 atomic force microscope

and a KEYENCE VK-X laser scanning confocal microscope. Surface images obtained from both methods were flattened by a polynomial background subtraction. Root mean square roughness S_q of the measured surface with an area A was calculated from

$$S_q = \sqrt{\frac{1}{A}\iint\limits_A z^2(x,y)dxdy}.$$

Photoluminescence measurements: Static PL spectra were measured on encapsulated perovskite layers deposited on soda lime glass substrate or ITO-coated glass substrate with NiO_x layer using an Andor SR303i-B spectrometer equipped with a silicon detector DU420A-BR-DD (iDus) after excitation with a 445 nm CW-laser (~20 mW/cm^2), spot size ~100 µm^2. Transient PL with 100 µm^2 excitation spot size was acquired using a TCSPC system (Becker&Hickl SPC130 with a multichannel detector: PML-16-C-1) after excitation with a PicoQuant PDL800B at 470 nm with a typical fluence as denoted between 70 and 2100 nJ/cm^2 at a repetition rate of 500 kHz. PL lifetime of the obtained data was calculated by using biexponential decay function (1); the mean lifetime τ_m was calculated using equation (2) with τ_1 and τ_2 being the fast and slow time component, respectively:[41]

(**1**) $$f(t) = A_1 exp\left(-\frac{t}{\tau_1}\right) + A_2 exp\left(-\frac{t}{\tau_2}\right)$$

(**2**) $$\tau_m = \frac{A_1\tau_1^2 + A_2\tau_2^2}{A_1\tau_1 + A_2\tau_2}$$

Locally resolved PL maps were recorded on perovskite samples deposited on ITO-coated glass substrate containing a thin PMMA film on top of the perovskite layer using a fiber coupled confocal microscopy setup. Excited with a diode laser (635 nm) with 1 µm^2 spot size, applying a continuous-wave photon flux of 1.7×10^{23} photons/(s cm^2), the emitted light was detected spectrally resolved using a diffraction grating (600 g/mm) and detected by a silicon charge

coupled device (Si-CCD). Optical components in the light path from laser to detector: laser band-pass filter 635 nm, cold-light mirror, sample, focusing lens with a numerical aperture of 0.9, cold-light mirror followed by 650 nm long-pass filter for suppressing spurious laser light, Ø 25 µm pinhole.

X-ray photoelectron spectroscopy: Measurements were conducted using an Al-K$_\alpha$ (1486.6 eV) source for excitation. The samples were transferred into the XPS setup in a dinitrogen filled container, which was directly attached to the XPS setup and evacuated. Therefore the samples were not exposed to air prior XPS measurements. All signals were fitted using Voigt peaks (15% Gaussian, 85% Lorentzian) and a linear background. The full-width at half maximum was the same for all peaks within the same orbital, with the exception of Ni 2p. For Ni 2p only the area of the Ni 2p$_{3/2}$ was fitted. The O 1s signal was fitted with three signals, one signal at 529.2 (NiO), a second signal with a binding energy of two electron volts above this one (NiOH), and a third signal at about three electron volts above the main peak. Br 3d was fitted using one signal for the Br 3d$_{5/2}$ and one for the Br 3d$_{3/2}$. The distance between these two was fixed to 1.1 eV and the area ratio to 0.67. I 3d, Cs 3d and Pb 4f were also fitted with two signals each for the respective 7/2 and 5/2, or 5/2 and 3/2 states. Area ratios and distances were not fixed, because the area ratios were within error range of 0.67 for the d-orbitals and 0.75 for the f orbital. *X-ray diffraction*: XRD pattern were recorded on a Bruker D8 for energy dispersive thin film analysis using grazing incidence geometry. The instrument is equipped with a Cu-anode (Kα1 = 1.54060 Å and Kα2 = 1.54443 Å), a Göbel mirror and a Sol-X energy dispersive single counter. XRD measurements were carried out in the 2θ range from 10° to 70° in 0.015° steps. The samples were static during the measurements to avoid extinction caused by a preferred direction of crystal growth.

Solar Cell Characterization. All current density–voltage (J–V), MPP and EQE measurements were undertaken in an MBRAUN N_2-filled glovebox with less than 0.1 ppm O_2 and H_2O. J–V measurements were conducted using an Oriel class ABB sun simulator, mimicking the AM1.5G spectrum with an intensity of 100 mW/cm^2 adjusted by the short-circuit current of a calibrated 2 × 2 cm silicon solar cell (Fraunhofer ISE). The active area of 0.16 cm^2 was defined by the overlap of orthogonal ITO and copper strips, both 4 mm in width. J–V curves of the solar cells were measured with a digital source meter (Keithley model 2400) in a two-wire configuration in two consecutive sweeps from −0.2 to 1.2 V and immediately afterwards backward from 1.2 to −0.2 V. The standard scan rate was 200 mV/s (voltage steps 0.02 V, settling time 50 ms, integration time 50 ms), but was varied between 10 mV/s and 10 V/s (for details see Table S2) for the scan rate dependent J–V measurement. For MPP tracking measurements the power output of a solar cell was continuously feedback controlled using homemade software. Starting at the voltage of the MPP of the backward J–V scan at 200 mV/s, steps of +10, 0, −10 mV were added to the actual voltage, while the current density of the device was traced at each operating point for 1 s. The bias point with the highest average power output during the last 0.5 s of each scan was then selected as the new MPP for the subsequent iteration. The external quantum efficiency (EQE) was measured using an Oriel Instruments QEPVSI-b system with a Xenon arc lamp (Newport 300 W, 66902) chopped at 35.5 Hz and a monochromator (Newport Cornerstone 260). The illumination beam size on the sample was 2.5 × 2.5 mm^2 and measurements were performed in a wavelength range from 300–850 nm with 10 nm steps, controlled by TracQ-Basic software. The EQE was measured without background illumination or applied bias voltage.

RESULTS AND DISCUSSION

Morphology Control of the Perovskite Layer

Perovskite layers were deposited by spin-coating of a precursor solution containing cesium iodide or cesium bromide, formamidinium iodide, lead(II) iodide and lead(II) bromide in DMF:DMSO (4:1), followed by drop-quenching with chlorobenzene (CBZ) and annealing at 100 °C in close analogy to previously reported procedures.[12,17,26] Although this method allows the deposition of continuous pin-hole free perovskite layers, we observed macroscopically matt and microscopically textured surfaces in contrast to shiny flat surfaces typically obtained with MAPbI$_3$. In the following we will discuss the influence of perovskite precursor composition, processing parameters, and perovskite precursor concentration on the resulting perovskite layer surface morphology after annealing.

Perovskite precursor composition

First, the formation of wrinkles was investigated by varying the composition of the perovskite precursor solution with respect to the ratio of Cs:FA and Br:I in $Cs_xFA_{1-x}Pb(I_{1-y}Br_y)_3$. Two series of $Cs_xFA_{1-x}Pb(I_{1-y}Br_y)_3$ perovskite layers with (1) x = 0–0.30 and y = 0.17 and (2) x = 0.15 and y = 0–0.30 were fabricated. In order to compare purely composition dependent changes, the perovskite precursor concentration (0.9 M) and processing parameters for these two series were kept constant (spin coating at 4000 rpm for 30s, CBZ drop-quenching after 10 s, annealing at 50°C for 1 min and 100 °C for 10 min). Figure 2 displays the root mean square (RMS) surface roughness that was obtained from confocal microscopy images (see Figures S1 and S2). We could find significant composition induced changes of the film roughness, i.e. wrinkle formation. In absence of either Cs or Br, such as $FAPb(I_{0.83}Br_{0.17})_3$ and $Cs_{0.15}FA_{0.85}PbI_3$, macroscopically shiny and microscopically flat (RMS = 32–43 nm) perovskite layers were obtained. These RMS

surface roughness values are slightly higher than 26.3 nm previously reported for solution processed flat MAPbI$_3$ layers.[42] In comparison, ultra-smooth MAPbI$_3$ layers with 8–12 nm RMS surface roughness were obtained using Pb(OAc)$_2$ as lead precursor,[43] while employing a combined gas-assisted and solvent drop-quenching method resulted as little as 2 nm RMS surface roughness.[44] In our study, wrinkles developed only if both two cations (Cs and FA) and two anions (I and Br) were present in the perovskite, in other words the combination of Cs and Br in FAPbI$_3$-based perovskite seems to induce the textured morphology. This can be seen by the strong increase in RMS surface roughness in Figure 2 when changing the composition regarding Cs content (dark grey bars) and Br content (orange bars). Generally, the surface roughness correlated with the concentration of Cs and Br. However, in comparison, cesium (RMS = 125 nm at 30 mol% Cs and 15 mol% Br) had stronger impact on the formation of wrinkles than bromide (RMS = 62 nm at 17 mol% Cs and 30 mol% Br). As all other fabrication parameters were kept constant, Cs and Br obviously influence the crystallization behavior of perovskite. Zhou *et al.* observed acceleration of the MAPb(I$_{1-x}$Br$_x$)$_3$ crystal growth with increasing bromide content.[45] As most basic explanation they suggested faster ion diffusion of bromide versus iodide based on the smaller ion radius of bromide. However, besides ion diffusion, crystal growth depends mainly on the availability of multinuclear lead(II) halide complexes which act as building blocks for bulk perovskite crystallites.[46] From a coordination chemistry perspective, bromide forms more stable complexes with lead(II) than iodide. This has been reported by Kamat and coworkers for [PbX$_3$]$^-$ and [PbX$_4$]$^{2-}$ with X = I, Br.[47] The impact of Cs$^+$ on perovskite precursor solution chemistry is yet unknown, but it may also shift the dynamic equilibrium of lead(II) halide species towards higher-order lead(II) halide complexes and thereby accelerate crystallization. Nevertheless, at low content (< 15 mol%; relative to lead) bromide alone cannot be made responsible for wrinkle formation, but the combination of both Br and Cs in Cs$_x$FA$_{1-x}$Pb(I$_{1-y}$Br$_y$)$_3$ seems to induce this unusual morphology.

To examine the formation of wrinkles and impact on solar cell performance, we used perovskite precursor solution with $Cs_{0.17}FA_{0.83}Pb(I_{0.83}Br_{0.17})_3$ stoichiometry for all further experiments. This established composition is among the most relevant for perovskite single junction and tandem solar cells and allowed us to compare optoelectronic data of thin films and photovoltaic data of solar cells with the literature.[26]
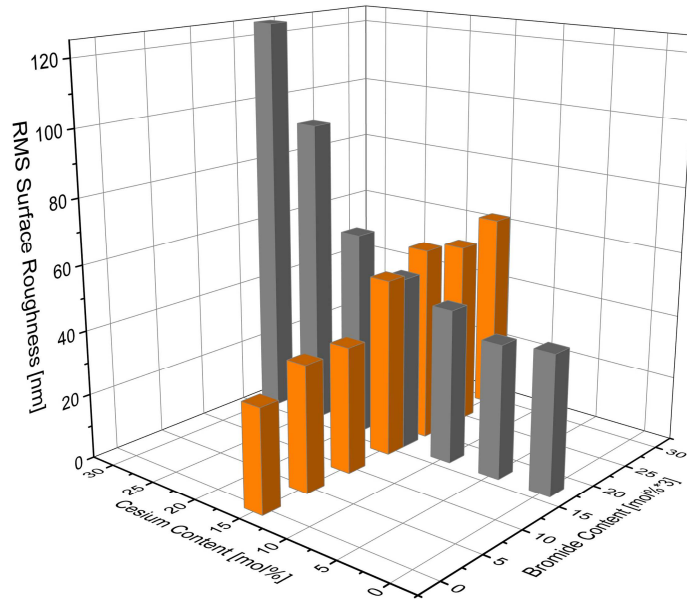

Figure 2: Root mean square (RMS) surface roughness obtained from confocal microscopy images of $Cs_xFA_{1-x}Pb(I_{1-y}Br_y)_3$ perovskite films (for images see Supporting Information, Figure S1 and S2) containing between 0 and 30 mol% bromide and cesium (relative to lead).

Processing parameters

To study the effect of perovskite layer morphology on optoelectronic properties and on the performance of solar cells, we developed two processing procedures for the given $Cs_{0.17}FA_{0.83}Pb(I_{0.83}Br_{0.17})_3$ perovskite composition. Optical, confocal and scanning electron microscopy (SEM) images of both perovskite morphologies are shown in Figure 1b-g. The first procedure, *P1,* yielded layers with flat morphology and rather smooth surface topography. The second procedure, *P2,* enabled a wrinkled morphology with clearly visible surface features as highlighted by the microscope images. The main difference between both procedures is a solvent-

poor atmosphere (open spin coater lid) and quick acceleration (4000 rpm, ramp 1 s) for P1, which resulted in the flat morphology, and a solvent-rich atmosphere (closed spin coater lid) and slow acceleration (two-step, 1000 rpm, then 6000 rpm) which generated the wrinkled morphology. In *P2*, two-step annealing was applied to obtain more uniformly structured perovskite layers. One step annealing equivalent to *P1* also gave wrinkles, but uniformity in surface roughness was much higher using two-step annealing. The same two-step annealing was also tested with *P1* which lead to a slightly reduced device performance but it had no effect on the morphology. For more processing condition details see Experimental Section.

To further analyze the different films, the layer thickness was determined from SEM images (Figure S3) and RMS surface roughness from confocal microscopy images (Figure S4a,b). The wrinkled perovskite morphology varied significantly in layer thickness between 500–1500 nm with RMS surface roughness of 250 nm. The flat morphology revealed a more uniform layer thickness of 290–380 nm and RMS roughness of 43 nm. Grain sizes of both samples were found to be relatively similar in the range of 50–400 nm, although cross-sectional SEMs showed much larger grains in the area of the wrinkles (see Figure S11). The grain size distribution in wrinkled perovskites is therefore spatially non-uniform. When following the perovskite film formation of *P1* in comparison to *P2* by eye, there was no visible difference in morphology after quenching with the anti-solvent chlorobenzene. However, within the first seconds of annealing the perovskite layer quickly developed a matt surface in case of *P2*, independent of the annealing temperature applied (> 50 °C). Formation of the flat shiny surface was observed on the same time scale employing *P1*. Notably, the wrinkled perovskite morphology seems to be energetically favored as this structure developed under the vast majority of processing conditions, although with varying height and lateral dimensions. Indeed, when adjusting the color scale of the confocal microscope image of the flat perovskite morphology (Figure S4b), also here small wrinkle-like pattern become visible (Figure S4e).

Perovskite precursor concentration

Another parameter found to strongly influence the perovskite layer morphology is the precursor concentration. Two series of perovskite layers were deposited from perovskite precursor solutions with concentration between 0.77–1.31 M using *P1* and *P2*, and their microstructure was analyzed by optical microscopy (Figure S5). All perovskite layers of these series were also tested in solar cells, performance data (PCE, J_{sc}, V_{oc}, and FF) are shown in Figure S6. Generally, the width and height of wrinkles, i.e. perovskite surface roughness, in either deposition procedure significantly increased with perovskite precursor solution concentration. When the procedure for flat films *P1* was employed, significant wrinkles developed at perovskite precursor solution concentration approximately larger 1 M. Therefore, the flat perovskite morphology is limited to precursor solutions with c < 1 M, equivalent to approximately d < 450 nm layer thickness. As the wrinkled morphology resulted in the highest device efficiency at around 0.9 M (Figure S6a), this concentration will be used as standard for both procedures in the following to give a fair comparison between both procedures. Note that no major difference in microstructural morphology, surface roughness and wrinkles, was observed when the perovskite film was crystallized on glass, polished silicon wafer, ITO, NiO_x, or PTAA. Thus, the substrate morphology, wettability thereof, and surface energy do not have a major influence on the crystallization behavior of this perovskite composition, meaning that the findings presented here are rather fundamental.

Summing up the morphological analysis, the surface roughness of $Cs_xFA_{1-x}Pb(I_{1-y}Br_y)_3$ perovskite layers with cesium and bromide content below 30 mol% (relative to Pb) is influenced by the perovskite precursor solution composition and concentration, and spin-coating parameters. From the experiments we can conclude the following four aspects: first, the formation of wrinkles in $Cs_xFA_{1-x}Pb(I_{1-y}Br_y)_3$ perovskite layers is strongly dependent on the content of

bromide and cesium, but to a smaller extent on that of bromide. Second, crystallization dynamics of perovskite precursor solutions with $Cs_{0.17}FA_{0.83}Pb(I_{0.83}Br_{0.17})_3$ composition tends to favor the wrinkled morphology, independent of substrate. Third, the perovskite surface roughness correlates with concentration of the perovskite precursor solution, which translates to layer thickness. Finally, the formation of wrinkles is suppressed by process *P1*, because quick rotational acceleration in an "open" environment (fast solvent evaporation) and early CBZ quenching yield a quick crystallization of a thin intermediate phase perovskite layer, which defines the final morphology. Interestingly, the phenomenon of wrinkled thin films on glass substrate is rare but commonly observed for sol-gel deposited ZnO layers.[48,49] In this case the folds develop during annealing of the wet precursor layer if the temperature is ramped up slowly. Furthermore, spinoidal decomposition by demixing of two phases has resulted similarly structured films of binary alloys and polymer blends.[50,51] However, we could not find any compositional inhomogeneity of the perovskite layer by global and local X-ray techniques (see sections below). Sveinbjörnsson *et al.*, who observed very similar morphological pattern in $MA_{0.15}FA_{0.85}Pb(I_{0.85}Br_{0.15})_3$ perovskite, suggested relaxation of strain in the perovskite precursor layer to be responsible for wrinkle formation based on different thermal expansion coefficients of perovskite and glass substrate.[30] In detail, they spin-coated perovskite solution on warm glass substrate and proposed that compressive strain is induced by cooling from solvent evaporation and injection of chlorobenzene. Our observations point to wrinkle formation during heat-up of the samples in the annealing step, a typical scenario for compressive strain built-up. Another possible source of compressive strain is volume expansion during perovskite crystallization from the Lewis base solvent-rich (DMSO, DMF) intermediate perovskite phase.[31,46,52] Independent of the exact origin of strain, any strain relaxation in a viscoelastic thin film, such as the semi-crystalline solvent-rich perovskite precursor phase might be described, can lead to plastic deformations, while in highly crystalline layers cracks would most likely occur.[53] Whether

deformations take place depends on the critical thickness of a thin film, as described in Thouless' strain model.[53] Briefly, thin layers withstand higher elastic strain than thick layers, which is in accordance with our observations (see concentration series in Figure S5). The effect of wrinkle formation is therefore suggested to be material and layer thickness dependent, which in turn translates to dependence on the chemical composition, precursor concentration and spin-coating speed, as has been demonstrated above. Thus, our findings point to the formation of the wrinkles influenced by compressive strain which is affected by composition, crystallization kinetics and layer thickness. The classical MAPbI$_3$ perovskite may not crystallize with wrinkled morphology because of lower strain during formation. We assume Cs (and Br) to have a significant influence on the material properties of FAPbI$_3$-based perovskites. The exact formation mechanism of wrinkles of mixed halide perovskites cannot be clarified without detailed in-situ film formation studies and data on the elastic properties on this perovskite composition, which is beyond the scope of this paper. Our findings are supported by work from Bush *et al*, who very recently suggested release of in-plane compressive strain during the intermediate phase of perovskite film formation to be responsible for wrinkle formation in Cs$_{0.17}$FA$_{0.83}$Pb(I$_{0.83}$Br$_{0.17}$)$_3$ layers.[31]

In order to analyze the impact of perovskite film morphology on solar cell performance, we processed p–i–n (so called inverted) perovskite solar cells with the structure as explained above and shown in Figure 1a. We chose this device design, as inverted devices show typically less pronounced hysteresis, it was previously successfully integrated into perovskite/silicon tandem architectures,[26] and also as the conformally grown top electron contact implemented here enables a fair comparison between different surface topographies. As hole selective contact, we utilized a ~15 nm thin layer of NiO$_x$ deposited by sol-gel method following the approach from You *et al*.[40] Figure S7 depicts atomic force microscopy images of NiO$_x$ on ITO-coated glass (RMS = 3.7 nm) compared to the bare ITO/glass substrate (RMS = 2.4 nm). X-ray photoelectron spectroscopy (XPS) revealed excellent agreement of the Ni 2p3/2 and O 1s core level spectra (Figure S8) with

the literature (Table S1). The O 1s spectrum showed a comparatively low content of hydroxide and oxyhydroxide species at a binding energy (BE) of 531.1 eV.[54] The O 1s peak at 532.4 eV can be assigned to nickel hydrate or organic species containing oxygen,[55] which is both similarly likely considering the use of hygroscopic ethylene glycol in the sol-gel deposition process in air. However, water in ALD deposited NiOx has also been reported at 533.4 eV BE.[56] Irrespective of the exact nature of the O 1s peak at 532.4 eV, XPS data indicate a high quality NiO_x layer with Ni 2p3/2 and O 1s spectra comparable to those of ALD deposited NiO_x which enabled 16.4% PCE perovskite solar cells.[56] On top of the hole selective layer, perovskite was deposited using *P1* or *P2*, as described before, and the solar cells were completed with thermal evaporation of fullerene-C_{60}, bathocuproine (BCP), and Cu forming the electron contact. Figure 3a displays the *J–V* curves under simulated AM1.5G illumination of the best devices processed according to procedure *P1* (blue data) in comparison the devices with wrinkled perovskite morphology when applying *P2* (red data). The *J–V* curves were recorded in both scanning directions from positive to negative bias (backward scan) and from negative to positive bias (forward scan). Both device types displayed negligible hysteresis at scan rates between 10 mV/s and 10 V/s (Figure S9 and Table S2) and stabilized power outputs very close to the respective *J–V* scans, as can be seen by maximum power point (MPP) tracking over five minutes (inset in Figure 3a) and by the open circles in the *J–V* scan. Figure 3b highlights the statistical distribution of 76 flat and 99 wrinkled solar cells together with Gaussian fits to the distribution which confirm the higher efficiency of devices with wrinkled perovskite morphology. The performance parameters of all devices are shown in Figure 3c and summarized as median and champion values in Table 1. The higher efficiency for wrinkled over flat films is realized by slightly enhanced J_{sc} from 20.1 to 21.0 mA/cm², slightly enhanced FF from 71.7 to 72.8%, and significantly enhanced V_{oc} from 0.88 to 1.00 V. The resulting efficiencies are 12.8 to 15.3% on median average and 14.7 to 17.0% at best for flat and wrinkled devices, respectively. We note that the overall efficiency is constrained

by the V_{oc} that is limited here to below 1.05 V. It has been recently shown that utilizing other hole transporting contact materials such as PTAA[23,57,58] or doped NiO_x layers enable higher V_{oc} potentials.[59–61] Thus, to our best knowledge the champion PCE of 17.0% presented here is among the best for mixed halide perovskite solar cells employing a non-doped and unmodified NiO_x contact layer presented so far.[62]
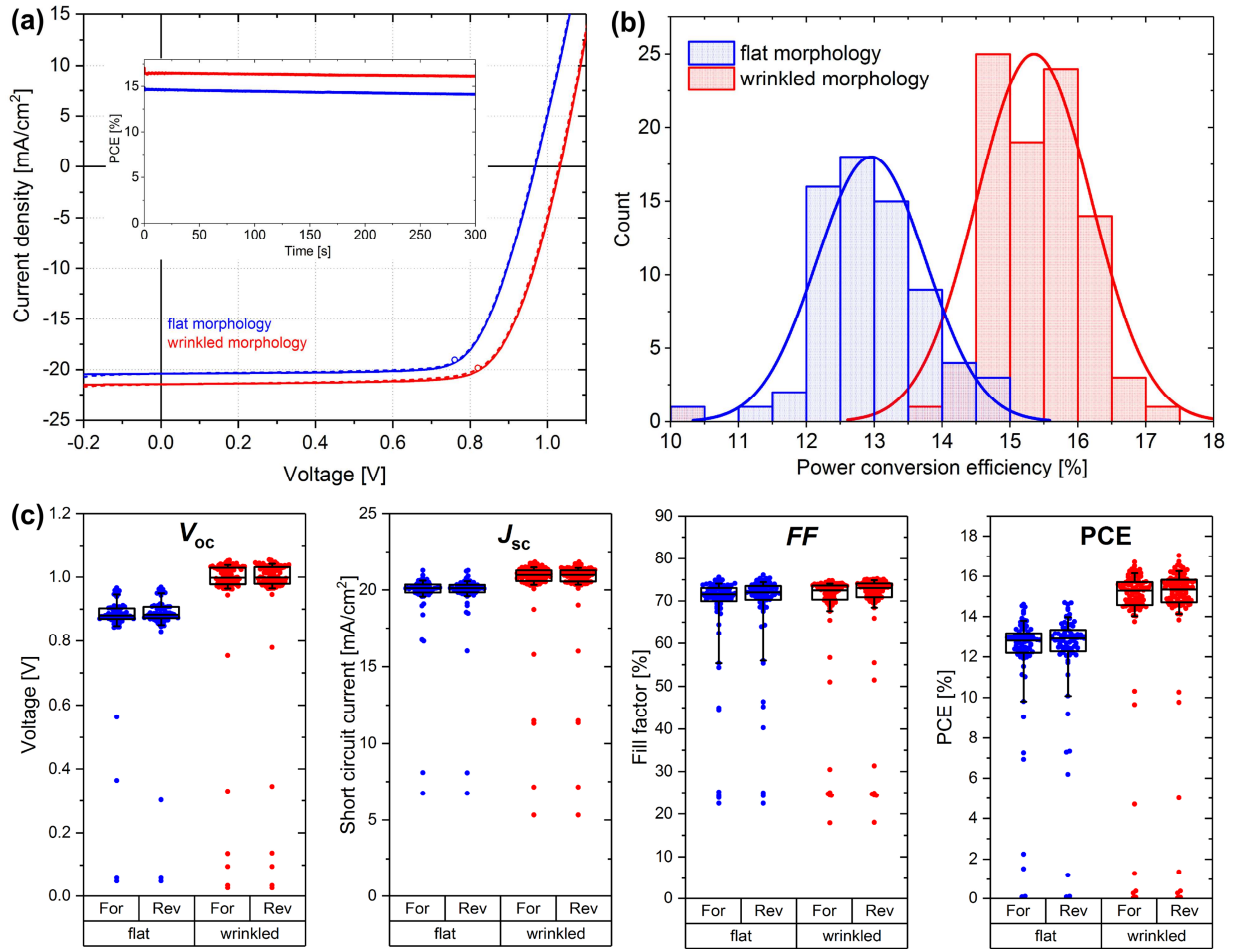

Figure 3: (a) *J–V* characteristics under simulated AM1.5G illumination for the best perovskite solar cells with flat (blue data) and wrinkled (red data) perovskite morphology in forward (−0.2 to 1.2 V; dashed lines) and backward (1.2 to −0.2 V; solid lines) scan direction at 0.2 V/s scan speed. Open circles in the respective color mark the MPP after 60 s of MPP tracking measurements (see inset). (b) Histogram of the PCE of devices with flat (blue columns) and wrinkled (red columns) perovskite morphology obtained from *J–V* measurements in backward scan direction. Blue and red lines represent Gaussian fits of the respectively colored data. (c) Statistical analysis of photovoltaic parameters from *J–V* measurements in forward and backward scan direction of 76 solar cells with flat perovskite morphology (blue data) and 99 solar cells with wrinkled perovskite morphology (red data). Boxes show range of 25–75% probability with median line, whiskers represent range of 10–90% probability.

Table 1: Parameters extracted from current–voltage characterization in backward scan direction at 0.2 V/s scan speed under simulated AM1.5G illumination of 76 solar cells with flat perovskite morphology and 99 solar cells with wrinkled perovskite morphology. The reported J_{sc}s are from *J-V* measurements, the values presented in brackets are from wavelength-integrated EQE × AM1.5G illumination spectra.

Morphology		V_{oc} [mV]	J_{sc} ($J_{sc\text{-}EQE}$) [mA/cm^2]	FF [%]	PCE [%]
Flat	**Champion**	968	20.4 (20.2)	74.4	14.7
	Median	881	20.1 (20.2)	71.7	12.8
Wrinkled	**Champion**	1042	21.8 (21.2)	75.0	17.0
	Median	999	21.0 (21.1)	72.8	15.3

To understand the changes in performance metrics we analyzed the external quantum efficiency (EQE) and the optical features of both perovskite absorber morphologies and summarized the data in Figure 4. From the SEM cross section displayed in Figures S3 we observed that the average perovskite film thickness is much higher for the wrinkled film with thicknesses up to 1.5 µm at the wrinkle position. Thus, it is reasonable that the higher J_{sc} for the wrinkled solar cells can be attributed to higher absorption in the perovskite films. Figure 4a shows the EQE spectra for various flat and wrinkled films. Especially in the long wavelength range, where the perovskite absorption is weaker,[63] the EQE of the wrinkled films is higher. The $J_{sc\text{-}EQE}$ from the integrated EQE spectra (Table 1) nicely fit to the J_{sc} measured under simulated AM1.5G illumination. Thus, the enhancement in J_{sc} from flat to wrinkled perovskite morphology is a purely optical feature of higher absorption. This is also reflected by the film absorption (Figure 4b) which was calculated from transmission and reflection spectra recorded on flat and wrinkled perovskite films on ITO-coated glass. At longer wavelengths between 500 nm and the respective band-gap edge around 750 nm, the thicker, wrinkled films absorb more light. Therefore, these films are able to generate on average approximately 1 mA/cm² more, as it was found from the *J–V* scans. Thus, we analyzed the different device stacks by optical simulations. In the simulation, we only consider flat interfaces and use an average perovskite layer thickness (for the wrinkled

case) to quantify the effect of possible light trapping as deviation between simulation and experiment. Figure S10 shows the simulation results. First, to reproduce the minor interference, we had to exclude/reduce coherence in the perovskite absorber layer in the simulation, especially for the flat films, as here interference is more visible due to the thinner film thickness. Therefore reduction of coherence caused by the lateral difference in film thickness is even more pronounced in the wrinkled films, though not visible in the EQE due to the high absorption of the thicker film. Second, in accordance with the experimental reflection and absorbance data, the simulated EQE is only enhanced for wavelength above 550 nm wavelength for the thicker wrinkled films. Thus, the slightly higher EQE found in Figure 4a in the wavelength range between 350 and 500 nm is most likely caused by slightly higher collection efficiency for the wrinkled film which is in agreement with the Urbach energy[39] and PL lifetime (see below). Third, the amount of photocurrent enhancement found for the thicker (wrinkled) films in the simulation matches quantitatively to the experiment with a slightly higher EQE measured between 600 and 750 nm wavelength as compared to the simulation for the wrinkled case. Consequently, most of the photocurrent gain measured for wrinkled films is originated in the thicker (average) absorber layer and only marginally by the wrinkled interfaces. This can be further confirmed by considering our recent results, where we have shown that sinusoidal textures can significantly enhance the photocurrent by 1 mA/cm² in both sub-cells of perovskite/silicon tandem solar cells for aspect ratios of 0.5.[64] The wrinkles formed here can in first order also be approximated by sinusoidal functions. However, the aspect ratio for the wrinkles formed here is rather small and in the order of 0.025 to 0.1. With that, the photocurrent gain would rather be minor in the order of 0.1 mA/cm² over fully flat surfaces in the tandem solar cell when surface is only textured by wrinkles on the µm scale and nano-roughness due to the perovskite grains is neglected.[64] Nonetheless, the ability to reduce interference, especially for the NIR wavelength region, due to the wrinkles will potentially play a more significant role in optimized perovskite/silicon tandem

devices with thicker perovskite layers (>1 µm) that need to be implemented to generate current

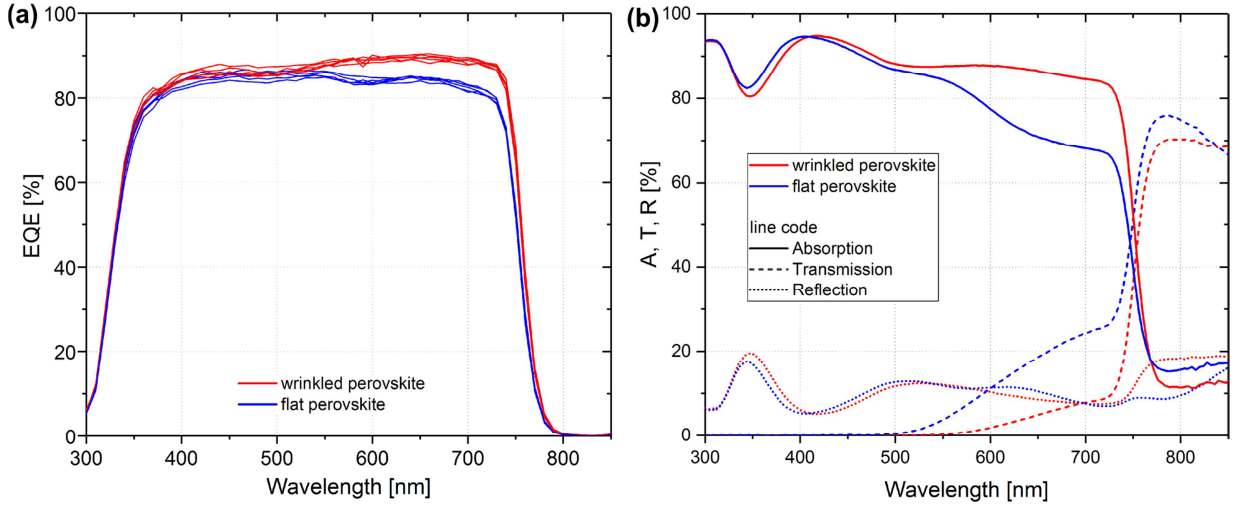matching when higher perovskite band-gaps are utilized.[65]

Figure 4: (a) External quantum efficiency (EQE) spectra of solar cells with flat (blue data, 5 devices, average integrated J_{sc} = 20.2 ± 0.3 mA/cm^2) and wrinkled (red data; 5 devices, average integrated J_{sc} = 21.1 ± 0.1 mA/cm^2) perovskite morphology. (b) UV/vis/NIR absorption, transmission and reflection spectra of perovskite layers with flat (blue lines) and wrinkled morphology (red lines).

Interestingly, we measured a significant improvement of more than 100 mV (on average) in V_{oc}

with the wrinkled formation indicating differences in recombination at either the perovskite/C$_{60}$

or the NiO$_x$/perovskite interface, or within the bulk of the perovskite absorber. Recently, it was

shown that inserting insulating layers in between the perovskite and fullerene-C$_{60}$ enable a much

higher open circuit voltage due to suppression of non-radiative recombination.[23] However, the

voltage here appears to be mainly limited from the NiO$_x$/perovskite interface as typical voltages

with organic p-type polymer such as PTAA as the hole transport layer enabled open circuit

voltages above 1.1 V.[23] Changes in valence band energy at the NiO$_x$/perovskite interface have

been reported for differently synthesized NiO$_x$[59–61] or surface modified NiO$_x$,[66,67] therefore the

exact band alignment and surface recombination at this interface might affect the V_{oc}

enhancement for the wrinkled over the flat films here. To analyze if the changed optoelectronic

properties are causing the voltage change, we studied the photoluminescence (PL) of films

processed with *P1* and *P2* on ITO-coated glass substrate with NiO$_x$ layer and on blank soda lime

glass. Steady-state PL spectra were recorded for both perovskite morphologies (Figure 5a) with peak maxima at 1.60 eV for the flat and 1.62 eV for the wrinkled perovskite. In comparison, a band gap of 1.63 eV for both perovskite morphologies was obtained from $(\alpha h v)^2$-plots of the optical absorption data assuming a direct allowed band gap (Figure S11). A more detailed analysis of the absorption edge by variable angle ellipsometry revealed slightly higher Urbach energies for flat $Cs_xFA_{1-x}Pb(I_{1-y}Br_y)_3$ perovskite layers indicative of somewhat higher lattice disorder.[39] Small differences in the quality of bulk perovskite material of flat and wrinkled samples were also reflected in PL lifetime. Charge carrier lifetimes were obtained by time-resolved photoluminescence (TRPL) spectroscopy of perovskite layers on glass/ITO/NiO_x (Figure 5b) and soda lime glass (Figure 5c) using biexponential decay fits.[68] The mean TRPL lifetimes τ_m of the neat layers on glass substrate show a similar decay time, 173 ns for the flat and 203 ns for the wrinkled films at 330 nJ/cm^2 excitation fluence (Table 2). For comparison, TRPL data with 70 and 2100 nJ/cm^2 excitation fluence were also recorded and are shown in Figure S12. Generally, the TRPL signal of all samples with wrinkled perovskite morphology decayed slower, suggesting lower non-radiative trap-assisted recombination. Even more evident, in the case with the NiO_x hole-transport layer present, the TRPL signal of flat perovskite samples decays much quicker than on glass, consistent with a higher recombination at the HTL/perovskite interface.[69,70] We assume this to affect, at least partially, the ~100 mV lower average V_{oc} measured for devices with flat perovskite morphology. Perovskite deposition procedure *P1* obviously does not promote formation of a suitable NiOx/perovskite interface for high V_{oc} devices.
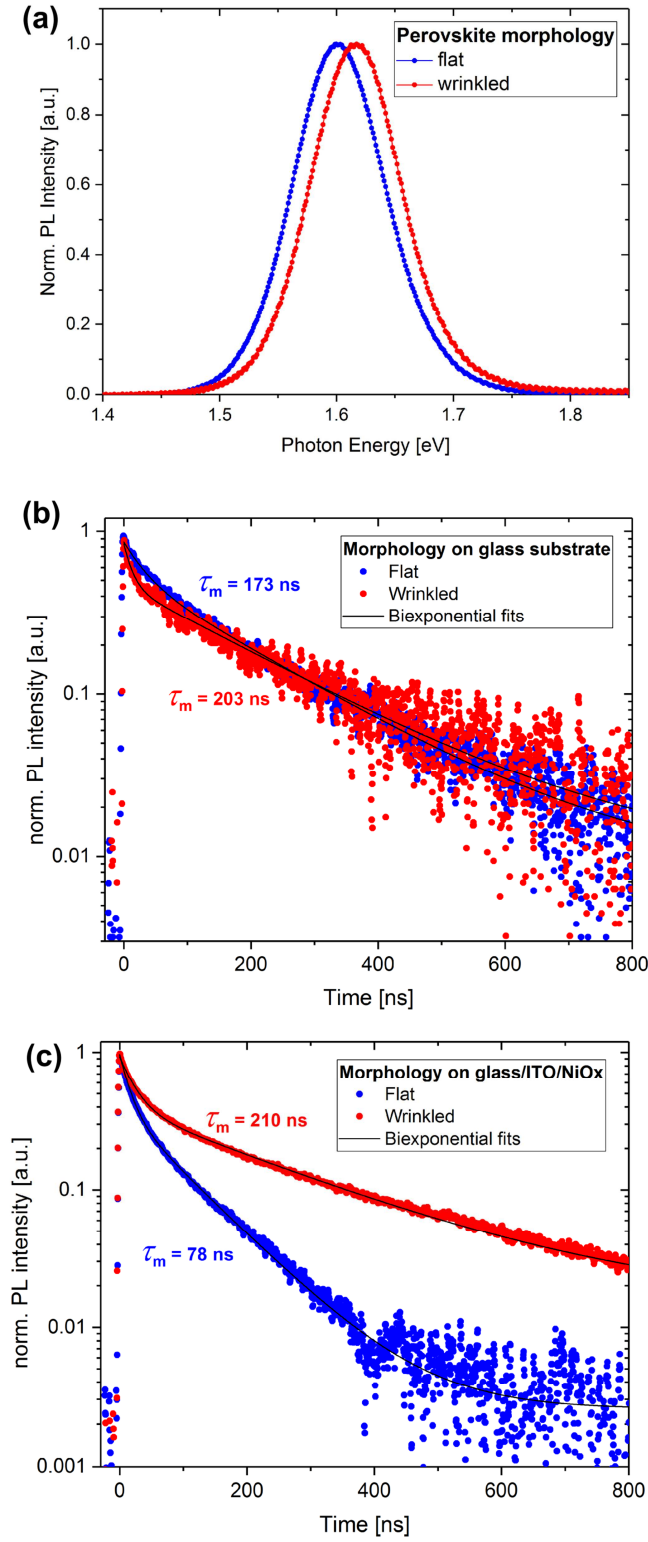
Figure 5: PL data of perovskite layers with flat (blue data) and wrinkled morphology (red data) on glass/ITO/NiO$_x$ (a, c) and soda lime glass (b) excited at 445 or 470 nm: (a) Steady-state PL (b, c) time-resolved PL decay curves at 330 nJ/cm^2 excitation fluence.

Table 2: Time constants of charge carrier lifetimes obtained by biexponential decay fits of TRPL data of perovskite layers with flat and wrinkled morphology on soda lime glass and glass/ITO/NiO$_x$ substrate (Figure 5). τ_m is the averaged time constant, τ_1 the fast and τ_2 the slow component.

Perovskite Sample	Substrate	τ_m [ns]	τ_1 [ns]	τ_2 [ns]
Flat	Glass	173	32	187
	Glass/ITO/NiO$_x$	78	15	94
Wrinkled	Glass	203	14	213
	Glass/ITO/NiO$_x$	210	24	236

To further illustrate the correlation between PL peak energy and morphology, using a confocal microscopic PL spectroscopy setup, PL maps were recorded of areas of which SEM images were taken beforehand, allowing superposition of SEM images and PL maps as shown in Figure 6. The match between the PL energy peak map and the SEM images is quite remarkable (Figure 6e), showing that the wrinkled morphology has different emission features exactly in the thin "valley" and thicker "hill" regions. Elevated regions correspond to peak positions at lower energies, whereas the valley regions exhibit peaks at higher energies, with a spectral difference of about 0.03 eV (Figure 6d). In contrast, much more uniform maps were recorded on samples with flat perovskite morphology (Figure 6c). Note that the PL peak position shifts slightly to lower values under constant illumination for the local PL measurements for both morphologies over several 100 s (see Figure S13) and the illumination time for the PL mapping is <1 s. Therefore a slight deviation in PL peak position is measured between global (Figure 5a) and local PL (Figure 6 c,d) data, presumably also as different excitation intensities were used. Having a mixed anion perovskite absorber, one conceivable explanation is compositional difference in form of increased bromide content in the flat regions (higher band gap valleys) and increased iodine content in the elevated areas (lower band gap hills).
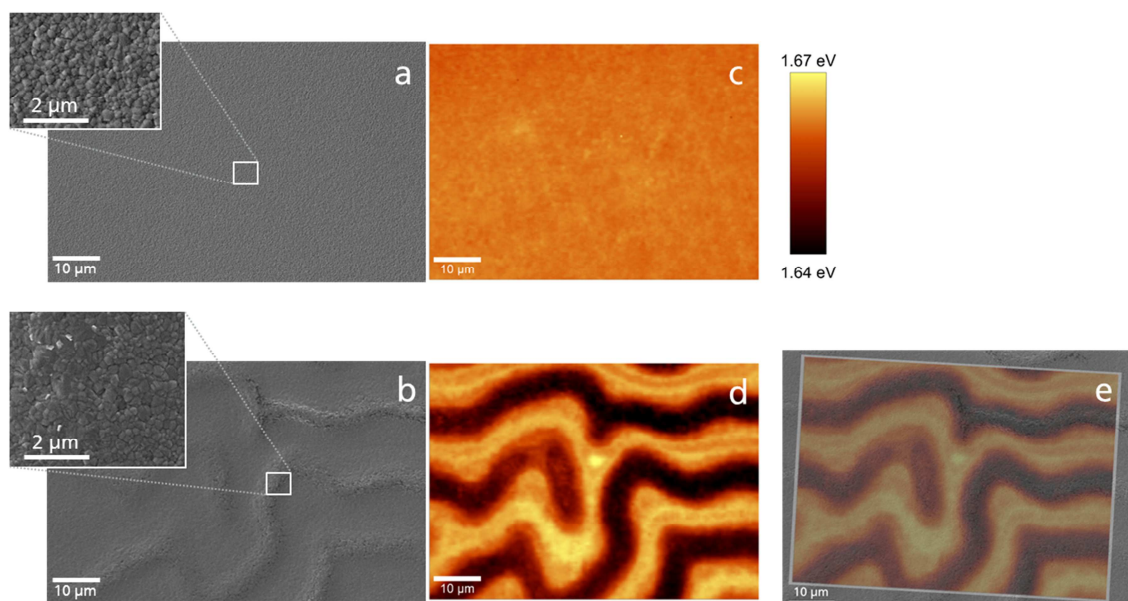
Figure 6: (a-b) SEM top view images of flat and wrinkled perovskite films on ITO-coated glass substrates. Insets show magnified areas of flat/wrinkled surfaces. (c-d) Spectral PL peak position (Voigt fit function) maps obtained in the same region as the SEM images. (e) Superposition of SEM image and PL peak position map for the wrinkled perovskite morphology. The band gap scale corresponds to all PL maps (c,d,e).

In order to test the hypothesis of compositional variation in the structured perovskite films as a possible cause of the inhomogeneous bandgap, energy dispersive X-ray spectroscopy (EDX) measurements were performed on cross sections of wrinkled perovskite layers. An EDX line scan ranging from a valley to hill area is shown in Figure 7. Within the measurement accuracy, no indication for a compositional variation can be found for the relevant elements. A presumed change in the bromide/iodide ratio was thus not confirmed. EDX spectra for the start (valley) and end point (hill) of the cross section of the wrinkled film can be found in Figure S14. EDX measurements in top view show similar results, the only significant difference being the detection of indium from ITO in thin layer areas, both for the flat films and the valleys of the wrinkled films (Figure S15). Additionally, X-ray diffraction (XRD) patterns (Figure S16) and XPS spectra (Figure S17) were recorded on films of both perovskite morphologies. The XRD patterns of the flat and wrinkled film morphology were consistent with a cubic perovskite crystal structure with lattice parameters varying slightly from 6.28 Å for the flat morphology to about 6.27 Å for the wrinkled film morphology. Low intensity ITO peaks are visible in the XRD pattern of the flat

morphology sample due to a thinner perovskite layer. Asymmetric broadening of the peaks at 13-14° of both samples was caused by the grazing incident setup and has also been observed with other perovskite samples with this instrument. XPS signals of Pb 4f, I 3d, Cs 3d and Br 3d of both morphologies were almost identical in binding energy and intensity (Figure S17 and Table S3), confirming very similar composition. The spectra closely resemble XPS data of $Cs_{0.2}FA_{0.8}Pb(I_{0.92}Br_{0.08})_3$ perovskite reported by Yi *et al.*[17] Thus, no clear evidence was found that the lateral PL peak shifts is caused by another perovskite phase or a different composition.
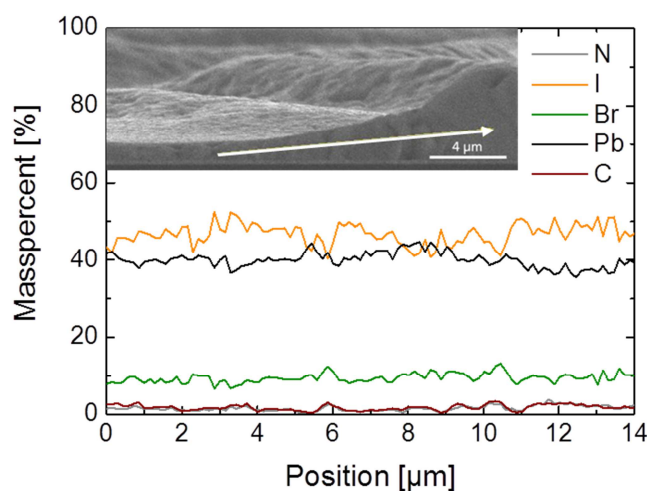

Figure 7: EDX line scan from flat to elevated area on a cross section of wrinkled perovskite film on ITO-coated glass substrate.

After finding that composition and perovskite phase are homogeneous in the wrinkled films, the grain size was analyzed in more detail: Regions of high layer thickness in the wrinkled perovskite layers systematically show larger grain sizes, not only on the surface but also within the film as cross section SEM images shown in Figure S14a,b. The correlation between crystal size and PL peak position has been observed for $MAPbI_3$ perovskite films as well as single crystals.[71–76] Accordingly, an increase crystal or grain size can be accompanied with a red-shift of the PL peak which has been attributed to higher lattice strain in small crystals by D'Innocenzo.[71] Another explanation of this effect is spectrally dependent reabsorption of photoluminescence radiation which may influence the peak position of the PL signal. In areas of high layer thickness,

enhanced reabsorption of higher energy photons may shift the measured peak position towards lower energies.

CONCLUSIONS

In summary, we analyzed the influence of $Cs_xFA_{1-x}Pb(I_{1-y}Br_y)_3$ precursor composition (x = 0–0.3; y = 0–0.3), concentration (0.7–1.3 M) and spin-coating conditions on the final morphology of perovskite thin films. Compositions containing both Cs and Br, besides FA and I, were found to form a wrinkled morphology under various processing conditions, in particular, if a high content of Cs was present. We were also able to generate flat perovskite layers using spin-coating parameters that suppress formation of the wrinkled structure. Using deposition procedures *P1* and *P2* for flat and wrinkled $Cs_{0.17}FA_{0.83}Pb(I_{0.83}Br_{0.17})_3$ perovskites, respectively, we then compared the photovoltaic performance of both morphologies in planar p-i-n solar cells. Devices with wrinkled perovskite morphology resulted in best solar cells with 17% PCE, while J_{sc} and V_{oc} limited the performance of devices with flat perovskite morphology to max. 14.7% PCE. Optical simulations showed that the significantly lower layer thickness of flat-structured perovskite accounts for most of the reduction in J_{sc}. Transient PL measurements of flat perovskite layers revealed high recombination at the NiO_x/perovskite interface accounting for the reduced V_{oc} of devices with flat perovskite morphology. This may be caused by the fast perovskite crystallization in deposition procedure *P1*. Despite differences of the peak position in PL maps dependent on the microscopic features, XRD, XPS and EDX analyses on macroscopic and microscopic level indicated the presence of a single, homogenous perovskite phase for both flat and wrinkled layers analyzed here. The observed PL red shift at areas of high layer thickness might be caused by grain size dependent lattice strain or thickness dependent reabsorption of PL radiation. Based on our observations on $Cs_xFA_{1-x}Pb(I_{1-y}Br_y)_3$ film formation, we propose that wrinkles result from the release of compressive strain within the perovskite layer, which is

strongly dependent on chemical composition, crystallization kinetics and layer thickness. This causal link is expected be relevant for further studies when utilizing mixed cation mixed halide perovskite compositions. As the wrinkle formation is strongly dependent on the perovskite precursor concentration, perovskite composition, and is especially enhanced with higher Cs or Br content, it should be taken into account when tuning the band gap towards 1.75 eV for multi-junction solar cell applications.

ACKNOWLEDGMENT

SUPPORTING INFORMATION

Optical microscope images, confocal microscope images, surface and cross-sectional scanning microscope images, atomic force microscopy images, X-ray photoelectron spectroscopy data, energy-dispersive X-ray spectroscopy data, X-ray diffraction pattern of perovskite samples. $(\alpha h\nu)^2$-plot, simulated EQE spectra and simulation details, *J-V* curves are various scan rates, and performance parameters of PSCs fabricated with different perovskite precursor concentrations. The Supporting Information is available free of charge on the ACS Publications website at DOI: XXX

REFERENCES

(1)   Kojima, A.; Teshima, K.; Shirai, Y.; Miyasaka, T. Organometal Halide Perovskites as Visible-Light Sensitizers for Photovoltaic Cells. *J. Am. Chem. Soc.* **2009**, *131*, 6050–6051.

(2)   Yang, W. S.; Park, B.-W.; Jung, E. H.; Jeon, N. J.; Kim, Y. C.; Lee, D. U.; Shin, S. S.; Seo, J.; Kim, E. K.; Noh, J. H.; et al. Iodide Management in Formamidinium-Lead-Halide–based Perovskite Layers for Efficient Solar Cells. *Science* **2017**, *356*, 1376–1379.

(3)   Green, M. A.; Ho-Baillie, A. Perovskite Solar Cells: The Birth of a New Era in Photovoltaics. *ACS Energy Lett.* **2017**, *2*, 822–830.

(4)   Green, M. A.; Hishikawa, Y.; Dunlop, E. D.; Levi, D. H.; Hohl-Ebinger, J.; Ho-Baillie, A. W. Y. Solar Cell Efficiency Tables (Version 51). *Prog. Photovoltaics Res. Appl.* **2018**, *26*, 3–12.

(5)   Manser, J. S.; Christians, J. A.; Kamat, P. V. Intriguing Optoelectronic Properties of Metal Halide Perovskites. *Chem. Rev.* **2016**, *116*, 12956–13008.

(6)   Unger, E. L.; Kegelmann, L.; Suchan, K.; Sörell, D.; Korte, L.; Albrecht, S. Roadmap and Roadblocks for the Band Gap Tunability of Metal Halide Perovskites. *J. Mater. Chem. A* **2017**, *5*, 11401–11409.

(7)   Petrus, M. L.; Schlipf, J.; Li, C.; Gujar, T. P.; Giesbrecht, N.; Müller-Buschbaum, P.; Thelakkat, M.; Bein, T.; Hüttner, S.; Docampo, P. Capturing the Sun: A Review of the Challenges and Perspectives of Perovskite Solar Cells. *Adv. Energy Mater.* **2017**, *7*, 1700264.

(8)   Song, Z.; McElvany, C. L.; Phillips, A. B.; Celik, I.; Krantz, P. W.; Watthage, S. C.; Liyanage, G. K.; Apul, D.; Heben, M. J. A Technoeconomic Analysis of Perovskite Solar

Module Manufacturing with Low-Cost Materials and Techniques. *Energy Environ. Sci.* **2017**, *10*, 1297–1305.

(9) Hörantner, M. T.; Snaith, H. J. Predicting and Optimising the Energy Yield of Perovskite-on-Silicon Tandem Solar Cells under Real World Conditions. *Energy Environ. Sci.* **2017**, *10*, 1983–1993.

(10) Lal, N. N.; Dkhissi, Y.; Li, W.; Hou, Q.; Cheng, Y.-B.; Bach, U. Perovskite Tandem Solar Cells. *Adv. Energy Mater.* **2017**, *7*, 1602761.

(11) Shin, S. S.; Yeom, E. J.; Yang, W. S.; Hur, S.; Kim, M. G.; Im, J.; Seo, J.; Noh, J. H.; Seok, S. Il. Colloidally Prepared La-Doped BaSnO 3 Electrodes for Efficient, Photostable Perovskite Solar Cells. *Science* **2017**, *356*, 167–171.

(12) Saliba, M.; Matsui, T.; Seo, J.-Y.; Domanski, K.; Correa-Baena, J.-P.; Nazeeruddin, M. K.; Zakeeruddin, S. M.; Tress, W.; Abate, A.; Hagfeldt, A.; et al. Cesium-Containing Triple Cation Perovskite Solar Cells: Improved Stability, Reproducibility and High Efficiency. *Energy Environ. Sci.* **2016**, *9*, 1989–1997.

(13) Yang, W. S.; Noh, J. H.; Jeon, N. J.; Kim, Y. C.; Ryu, S.; Seo, J.; Seok, S. I. High-Performance Photovoltaic Perovskite Layers Fabricated through Intramolecular Exchange. *Science* **2015**, *348*, 1234–1237.

(14) Conings, B.; Drijkoningen, J.; Gauquelin, N.; Babayigit, A.; D'Haen, J.; D'Olieslaeger, L.; Ethirajan, A.; Verbeeck, J.; Manca, J.; Mosconi, E.; et al. Intrinsic Thermal Instability of Methylammonium Lead Trihalide Perovskite. *Adv. Energy Mater.* **2015**, *5*, 1500477.

(15) Nickel, N. H.; Lang, F.; Brus, V. V.; Shargaieva, O.; Rappich, J. Unraveling the Light-Induced Degradation Mechanisms of CH3NH3PbI3 Perovskite Films. *Adv. Electron. Mater.* **2017**, *3*, 1700158.

(16) Rehman, W.; McMeekin, D. P.; Patel, J. B.; Milot, R. L.; Johnston, M. B.; Snaith, H. J.; Herz, L. M. Photovoltaic Mixed-Cation Lead Mixed-Halide Perovskites: Links between Crystallinity, Photo-Stability and Electronic Properties. *Energy Environ. Sci.* **2017**, *10*, 361–369.

(17) Yi, C.; Luo, J.; Meloni, S.; Boziki, A.; Ashari-Astani, N.; Grätzel, C.; Zakeeruddin, S. M.; Röthlisberger, U.; Grätzel, M. Entropic Stabilization of Mixed A-Cation ABX 3 Metal Halide Perovskites for High Performance Perovskite Solar Cells. *Energy Environ. Sci.* **2016**, *9*, 656–662.

(18) Jeon, N. J.; Noh, J. H.; Yang, W. S.; Kim, Y. C.; Ryu, S.; Seo, J.; Seok, S. Il. Compositional Engineering of Perovskite Materials for High-Performance Solar Cells. *Nature* **2015**, *517*, 476–480.

(19) Heo, J. H.; Song, D. H.; Han, H. J.; Kim, S. Y.; Kim, J. H.; Kim, D.; Shin, H. W.; Ahn, T. K.; Wolf, C.; Lee, T. W.; et al. Planar CH3NH3PbI3 Perovskite Solar Cells with Constant 17.2% Average Power Conversion Efficiency Irrespective of the Scan Rate. *Adv. Mater.*

2015, *27*, 3424–3430.

(20) Koh, T. M.; Fu, K.; Fang, Y.; Chen, S.; Sum, T. C.; Mathews, N.; Mhaisalkar, S. G.; Boix, P. P.; Baikie, T. Formamidinium-Containing Metal-Halide: An Alternative Material for Near-IR Absorption Perovskite Solar Cells. *J. Phys. Chem. C* **2014**, *118*, 16458–16462.

(21) Edri, E.; Kirmayer, S.; Cahen, D.; Hodes, G. High Open-Circuit Voltage Solar Cells Based on Organic–Inorganic Lead Bromide Perovskite. *J. Phys. Chem. Lett.* **2013**, *4*, 897–902.

(22) Kulbak, M.; Cahen, D.; Hodes, G. How Important Is the Organic Part of Lead Halide Perovskite Photovoltaic Cells? Efficient CsPbBr 3 Cells. *J. Phys. Chem. Lett.* **2015**, *6*, 2452–2456.

(23) Stolterfoht, M.; Wolff, C. M.; Amir, Y.; Paulke, A.; Perdigón-Toro, L.; Caprioglio, P.; Neher, D. Approaching the Fill Factor Shockley–Queisser Limit in Stable, Dopant-Free Triple Cation Perovskite Solar Cells. *Energy Environ. Sci.* **2017**, *10*, 1530–1539.

(24) Tan, H.; Jain, A.; Voznyy, O.; Lan, X.; García de Arquer, F. P.; Fan, J. Z.; Quintero-Bermudez, R.; Yuan, M.; Zhang, B.; Zhao, Y.; et al. Efficient and Stable Solution-Processed Planar Perovskite Solar Cells via Contact Passivation. *Science* **2017**, *355*, 722–726.

(25) Beal, R. E.; Slotcavage, D. J.; Leijtens, T.; Bowring, A. R.; Belisle, R. A.; Nguyen, W. H.; Burkhard, G. F.; Hoke, E. T.; McGehee, M. D. Cesium Lead Halide Perovskites with Improved Stability for Tandem Solar Cells. *J. Phys. Chem. Lett.* **2016**, *7*, 746–751.

(26) Bush, K. A.; Palmstrom, A. F.; Yu, Z. J.; Boccard, M.; Cheacharoen, R.; Mailoa, J. P.; McMeekin, D. P.; Hoye, R. L. Z.; Bailie, C. D.; Leijtens, T.; et al. 23.6%-Efficient Monolithic Perovskite/Silicon Tandem Solar Cells with Improved Stability. *Nat. Energy* **2017**, *2*, 17009.

(27) McMeekin, D. P.; Sadoughi, G.; Rehman, W.; Eperon, G. E.; Saliba, M.; Horantner, M. T.; Haghighirad, A.; Sakai, N.; Korte, L.; Rech, B.; et al. A Mixed-Cation Lead Mixed-Halide Perovskite Absorber for Tandem Solar Cells. *Science* **2016**, *351*, 151–155.

(28) Kim, J.; Saidaminov, M. I.; Tan, H.; Zhao, Y.; Kim, Y.; Choi, J.; Jo, J. W.; Fan, J.; Quintero-Bermudez, R.; Yang, Z.; et al. Amide-Catalyzed Phase-Selective Crystallization Reduces Defect Density in Wide-Bandgap Perovskites. *Adv. Mater.* **2018**, 1706275.

(29) Jacobsson, T. J.; Correa-Baena, J.-P.; Pazoki, M.; Saliba, M.; Schenk, K.; Grätzel, M.; Hagfeldt, A. Exploration of the Compositional Space for Mixed Lead Halogen Perovskites for High Efficiency Solar Cells. *Energy Environ. Sci.* **2016**, *9*, 1706–1724.

(30) Sveinbjörnsson, K.; Aitola, K.; Zhang, J.; Johansson, M. B.; Zhang, X.; Correa-Baena, J.-P.; Hagfeldt, A.; Boschloo, G.; Johansson, E. M. J. Ambient Air-Processed Mixed-Ion Perovskites for High-Efficiency Solar Cells. *J. Mater. Chem. A* **2016**, *4*, 16536–16545.

(31) Bush, K. A.; Rolston, N.; Gold-Parker, A.; Manzoor, S.; Hausele, J.; Yu, Z. J.; Raiford, J.

A.; Cheacharoen, R.; Holman, Z. C.; Toney, M. F.; et al. Controlling Thin-Film Stress and Wrinkling during Perovskite Film Formation. *ACS Energy Lett.* **2018**, 1225–1232.

(32)   Brendel, R. *Thin-Film Crystalline Silicon Solar Cells: Physics and Technology*; Wiley-VCH, 2003.

(33)   Pascoe, A. R.; Meyer, S.; Huang, W.; Li, W.; Benesperi, I.; Duffy, N. W.; Spiccia, L.; Bach, U.; Cheng, Y.-B. Enhancing the Optoelectronic Performance of Perovskite Solar Cells via a Textured CH3NH3PbI3 Morphology. *Adv. Funct. Mater.* **2016**, *26*, 1278–1285.

(34)   Jošt, M.; Albrecht, S.; Kegelmann, L.; Wolff, C. M.; Lang, F.; Lipovšek, B.; Krč, J.; Korte, L.; Neher, D.; Rech, B.; et al. Efficient Light Management by Textured Nanoimprinted Layers for Perovskite Solar Cells. *ACS Photonics* **2017**, *4*, 1232–1239.

(35)   de Quilettes, D. W.; Vorpahl, S. M.; Stranks, S. D.; Nagaoka, H.; Eperon, G. E.; Ziffer, M. E.; Snaith, H. J.; Ginger, D. S. Impact of Microstructure on Local Carrier Lifetime in Perovskite Solar Cells. *Science* **2015**, *348*, 683–686.

(36)   Sharenko, A.; Toney, M. F. Relationships between Lead Halide Perovskite Thin-Film Fabrication, Morphology, and Performance in Solar Cells. *J. Am. Chem. Soc.* **2016**, *138*, 463–470.

(37)   Dar, M. I.; Hinderhofer, A.; Jacopin, G.; Belova, V.; Arora, N.; Zakeeruddin, S. M.; Schreiber, F.; Grätzel, M. Function Follows Form: Correlation between the Growth and Local Emission of Perovskite Structures and the Performance of Solar Cells. *Adv. Funct. Mater.* **2017**, *27*, 1701433.

(38)   Bi, D.; Luo, J.; Zhang, F.; Magrez, A.; Athanasopoulou, E. N.; Hagfeldt, A.; Grätzel, M. Morphology Engineering: A Route to Highly Reproducible and High Efficiency Perovskite Solar Cells. *ChemSusChem* **2017**, *10*, 1624–1630.

(39)   Tejada, A.; Braunger, S.; Korte, L.; Albrecht, S.; Rech, B.; Guerra, J. A. Optical Characterization and Bandgap Engineering of Flat and Wrinkle-Textured FA 0.83 Cs 0.17 Pb(I 1– x Br x) 3 Perovskite Thin Films. *J. Appl. Phys.* **2018**, *123*, 175302.

(40)   You, J.; Meng, L.; Song, T.-B.; Guo, T.-F.; Yang, Y.; Chang, W.-H.; Hong, Z.; Chen, H.; Zhou, H.; Chen, Q.; et al. Improved Air Stability of Perovskite Solar Cells via Solution-Processed Metal Oxide Transport Layers. *Nat. Nanotechnol.* **2015**, *11*, 75–81.

(41)   Wang, C.; Zhao, D.; Grice, C. R.; Liao, W.; Yu, Y.; Cimaroli, A.; Shrestha, N.; Roland, P. J.; Chen, J.; Yu, Z.; et al. Low-Temperature Plasma-Enhanced Atomic Layer Deposition of Tin Oxide Electron Selective Layers for Highly Efficient Planar Perovskite Solar Cells. *J. Mater. Chem. A* **2016**, *4*, 12080–12087.

(42)   Noel, N. K.; Habisreutinger, S. N.; Wenger, B.; Klug, M. T.; Hörantner, M. T.; Johnston, M. B.; Nicholas, R. J.; Moore, D. T.; Snaith, H. J. A Low Viscosity, Low Boiling Point, Clean Solvent System for the Rapid Crystallisation of Highly Specular Perovskite Films. *Energy Environ. Sci.* **2017**, *10*, 145–152.

(43) Zhang, W.; Saliba, M.; Moore, D. T.; Pathak, S. K.; Hörantner, M. T.; Stergiopoulos, T.; Stranks, S. D.; Eperon, G. E.; Alexander-Webber, J. A.; Abate, A.; et al. Ultrasmooth Organic–inorganic Perovskite Thin-Film Formation and Crystallization for Efficient Planar Heterojunction Solar Cells. *Nat. Commun.* **2015**, *6*, 6142.

(44) Xia, B.; Wu, Z.; Dong, H.; Xi, J.; Wu, W.; Lei, T.; Xi, K.; Yuan, F.; Jiao, B.; Xiao, L.; et al. Formation of Ultrasmooth Perovskite Films toward Highly Efficient Inverted Planar Heterojunction Solar Cells by Micro-Flowing Anti-Solvent Deposition in Air. *J. Mater. Chem. A* **2016**, *4*, 6295–6303.

(45) Zhou, Y.; Yang, M.; Game, O. S.; Wu, W.; Kwun, J.; Strauss, M. A.; Yan, Y.; Huang, J.; Zhu, K.; Padture, N. P. Manipulating Crystallization of Organolead Mixed-Halide Thin Films in Antisolvent Baths for Wide-Bandgap Perovskite Solar Cells. *ACS Appl. Mater. Interfaces* **2016**, *8*, 2232–2237.

(46) Guo, Y.; Shoyama, K.; Sato, W.; Matsuo, Y.; Inoue, K.; Harano, K.; Liu, C.; Tanaka, H.; Nakamura, E. Chemical Pathways Connecting Lead(II) Iodide and Perovskite via Polymeric Plumbate(II) Fiber. *J. Am. Chem. Soc.* **2015**, *137*, 15907–15914.

(47) Yoon, S. J.; Stamplecoskie, K. G.; Kamat, P. V. How Lead Halide Complex Chemistry Dictates the Composition of Mixed Halide Perovskites. *J. Phys. Chem. Lett.* **2016**, *7*, 1368–1373.

(48) Sekine, N.; Chou, C.-H.; Kwan, W. L.; Yang, Y. ZnO Nano-Ridge Structure and Its Application in Inverted Polymer Solar Cell. *Org. Electron.* **2009**, *10*, 1473–1477.

(49) Ryu, S. Y.; Seo, J. H.; Hafeez, H.; Song, M.; Shin, J. Y.; Kim, D. H.; Jung, Y. C.; Kim, C. S. Effects of the Wrinkle Structure and Flat Structure Formed During Static Low-Temperature Annealing of ZnO on the Performance of Inverted Polymer Solar Cells. *J. Phys. Chem. C* **2017**, *121*, 9191–9201.

(50) Léonard, F.; Desai, R. Spinodal Decomposition and Dislocation Lines in Thin Films and Bulk Materials. *Phys. Rev. B* **1998**, *58*, 8277–8288.

(51) Wang, W.; Shiwaku, T.; Hashimoto, T. Phase Separation Dynamics and Pattern Formation in Thin Films of a Liquid Crystalline Copolyester in Its Biphasic Region. *Macromolecules* **2003**, *36*, 8088–8096.

(52) Rong, Y.; Venkatesan, S.; Guo, R.; Wang, Y.; Bao, J.; Li, W.; Fan, Z.; Yao, Y. Critical Kinetic Control of Non-Stoichiometric Intermediate Phase Transformation for Efficient Perovskite Solar Cells. *Nanoscale* **2016**, *8*, 12892–12899.

(53) Thouless, M. D. Modeling the Development and Relaxation of Stresses in Films. *Annu. Rev. Mater. Sci.* **1995**, *25*, 69–96.

(54) Manders, J. R.; Tsang, S.; Hartel, M. J.; Lai, T.; Chen, S.; Amb, C. M.; Reynolds, J. R.; So, F. Solution-Processed Nickel Oxide Hole Transport Layers in High Efficiency Polymer Photovoltaic Cells. *Adv. Funct. Mater.* **2013**, *23*, 2993–3001.

(55) Mansour, A. N.; Melendres, C. A. Characterization of α-Ni(OH)2 by XPS. *Surf. Sci. Spectra* **1994**, *3*, 255–262.

(56) Seo, S.; Park, I. J.; Kim, M.; Lee, S.; Bae, C.; Jung, H. S.; Park, N.-G.; Kim, J. Y.; Shin, H. An Ultra-Thin, Un-Doped NiO Hole Transporting Layer of Highly Efficient (16.4%) Organic–inorganic Hybrid Perovskite Solar Cells. *Nanoscale* **2016**, *8*, 11403–11412.

(57) Zhao, J.; Zheng, X.; Deng, Y.; Li, T.; Shao, Y.; Gruverman, A.; Shield, J.; Huang, J. Is Cu a Stable Electrode Material in Hybrid Perovskite Solar Cells for a 30-Year Lifetime? *Energy Environ. Sci.* **2016**, *9*, 3650–3656.

(58) Chen, B.; Bai, Y.; Yu, Z.; Li, T.; Zheng, X.; Dong, Q.; Shen, L.; Boccard, M.; Gruverman, A.; Holman, Z.; et al. Efficient Semitransparent Perovskite Solar Cells for 23.0%-Efficiency Perovskite/Silicon Four-Terminal Tandem Cells. *Adv. Energy Mater.* **2016**, *6*, 1601128.

(59) Jung, J. W.; Chueh, C.-C.; Jen, A. K. Y. A Low-Temperature, Solution-Processable, Cu-Doped Nickel Oxide Hole-Transporting Layer via the Combustion Method for High-Performance Thin-Film Perovskite Solar Cells. *Adv. Mater.* **2015**, *27*, 7874–7880.

(60) Chen, W.; Wu, Y.; Yue, Y.; Liu, J.; Zhang, W.; Yang, X.; Chen, H.; Bi, E.; Ashraful, I.; Gratzel, M.; et al. Efficient and Stable Large-Area Perovskite Solar Cells with Inorganic Charge Extraction Layers. *Science* **2015**, *350*, 944–948.

(61) Chen, W.; Liu, F.-Z.; Feng, X.-Y.; Djurišić, A. B.; Chan, W. K.; He, Z.-B. Cesium Doped NiO x as an Efficient Hole Extraction Layer for Inverted Planar Perovskite Solar Cells. *Adv. Energy Mater.* **2017**, *7*, 1700722.

(62) Hu, C.; Bai, Y.; Xiao, S.; Zhang, T.; Meng, X.; Ng, W. K.; Yang, Y.; Wong, K. S.; Chen, H.; Yang, S. Tuning the A-Site Cation Composition of FA Perovskites for Efficient and Stable NiO-Based P–i–n Perovskite Solar Cells. *J. Mater. Chem. A* **2017**, *5*, 21858–21865.

(63) Guerra, J. A.; Tejada, A.; Korte, L.; Kegelmann, L.; Töfflinger, J. A.; Albrecht, S.; Rech, B.; Weingärtner, R. Determination of the Complex Refractive Index and Optical Bandgap of CH3NH3PbI3 Thin Films. *J. Appl. Phys.* **2017**, *121*, 173104.

(64) Chen, D.; Manley, P.; Tockhorn, P.; Eisenhauer, D.; Köppel, G.; Hammerschmidt, M.; Burger, S.; Albrecht, S.; Becker, C.; Jäger, K. Nanophotonic Light Management for Perovskite–silicon Tandem Solar Cells. *J. Photonics Energy* **2018**, *8*, 1.

(65) Jäger, K.; Korte, L.; Rech, B.; Albrecht, S. Numerical Optical Optimization of Monolithic Planar Perovskite-Silicon Tandem Solar Cells with Regular and Inverted Device Architectures. *Opt. Express* **2017**, *25*, A473.

(66) Bai, Y.; Chen, H.; Xiao, S.; Xue, Q.; Zhang, T.; Zhu, Z.; Li, Q.; Hu, C.; Yang, Y.; Hu, Z.; et al. Effects of a Molecular Monolayer Modification of NiO Nanocrystal Layer Surfaces on Perovskite Crystallization and Interface Contact toward Faster Hole Extraction and Higher Photovoltaic Performance. *Adv. Funct. Mater.* **2016**, *26*, 2950–2958.

(67) Chen, C.; Yang, G.; Ma, J.; Zheng, X.; Chen, Z.; Zhang, Q.; Fang, G. Surface Treatment via Li-Bis-(Trifluoromethanesulfonyl) Imide to Eliminate the Hysteresis and Enhance the Efficiency of Inverted Perovskite Solar Cells. *J. Mater. Chem. C* **2017**, *5*, 10280–10287.

(68) Liang, P.-W.; Liao, C.-Y.; Chueh, C.-C.; Zuo, F.; Williams, S. T.; Xin, X.-K.; Lin, J.; Jen, A. K.-Y. Additive Enhanced Crystallization of Solution-Processed Perovskite for Highly Efficient Planar-Heterojunction Solar Cells. *Adv. Mater.* **2014**, *26*, 3748–3754.

(69) Wolff, C. M.; Zu, F.; Paulke, A.; Toro, L. P.; Koch, N.; Neher, D. Reduced Interface-Mediated Recombination for High Open-Circuit Voltages in CH3NH3PbI3 Solar Cells. *Adv. Mater.* **2017**, *29*, 1700159.

(70) Abdi-Jalebi, M.; Andaji-Garmaroudi, Z.; Cacovich, S.; Stavrakas, C.; Philippe, B.; Richter, J. M.; Alsari, M.; Booker, E. P.; Hutter, E. M.; Pearson, A. J.; et al. Maximizing and Stabilizing Luminescence from Halide Perovskites with Potassium Passivation. *Nature* **2018**, *555*, 497–501.

(71) D'Innocenzo, V.; Kandada, A. R. S.; De Bastiani, M.; Gandini, M.; Petrozza, A. Tuning the Light Emission Properties by Band Gap Engineering in Hybrid Lead Halide Perovskite. *J. Am. Chem. Soc.* **2014**, *136*, 17730–17733.

(72) Quarti, C.; Grancini, G.; Mosconi, E.; Bruno, P.; Ball, J. M.; Lee, M. M.; Snaith, H. J.; Petrozza, A.; De Angelis, F. The Raman Spectrum of the CH3NH3PbI3 Hybrid Perovskite: Interplay of Theory and Experiment. *J. Phys. Chem. Lett.* **2014**, *5*, 279–284.

(73) Mastroianni, S.; Heinz, F. D.; Im, J.-H.; Veurman, W.; Padilla, M.; Schubert, M. C.; Würfel, U.; Grätzel, M.; Park, N.-G.; Hinsch, A. Analysing the Effect of Crystal Size and Structure in Highly Efficient CH3NH3PbI3 Perovskite Solar Cells by Spatially Resolved Photo- and Electroluminescence Imaging. *Nanoscale* **2015**, *7*, 19653–19662.

(74) Nie, W.; Tsai, H.; Asadpour, R.; Blancon, J.-C.; Neukirch, A. J.; Gupta, G.; Crochet, J. J.; Chhowalla, M.; Tretiak, S.; Alam, M. A.; et al. High-Efficiency Solution-Processed Perovskite Solar Cells with Millimeter-Scale Grains. *Science* **2015**, *347*, 522–525.

(75) Grancini, G.; D'Innocenzo, V.; Dohner, E. R.; Martino, N.; Kandada, A. R. S.; Mosconi, E.; De Angelis, F.; Karunadasa, H. I.; Hoke, E. T.; Petrozza, A. CH3NH3PbI3 Perovskite Single Crystals: Surface Photophysics and Their Interaction with the Environment. *Chem. Sci.* **2015**, *6*, 7305–7310.

(76) Grancini, G.; Kandada, A. R. S.; Frost, J. M.; Barker, A. J.; De Bastiani, M.; Gandini, M.; Marras, S.; Lanzani, G.; Walsh, A.; Petrozza, A. Role of Microstructure in the Electron–hole Interaction of Hybrid Lead Halide Perovskites. *Nat. Photonics* **2015**, *9*, 695–701.

TABLE OF CONTENT GRAPHIC